International Journal of Fracture **73:** 81–92, 1995.

Crack-particle interaction in a two-phase composite Part II: crack deflection

P. LIPETZKY[1] and Z. KNESL[2]
[1] *Department of Civil Engineering, Rensselaer Polytechnic Institute, Troy, New York, 12180-3590, USA.*
[2] *Czech Academy of Sciences, Institute of Physics of Materials, Zizkova 22, 616 62 Brno, Czech Republic*

Received 14 July 1994; accepted in revised form 13 March 1995

Abstract. A numerical analysis has been performed on a system involving a crack near a single particle with the objective of finding a general relation for the size and shape of the elastic, crack-particle interaction zone which necessarily exists near particles in two-phase composites. In order to quantify the zone boundaries, various crack-particle geometries were modelled and a single characterization parameter was developed. Results show that a zone in which the energy release rate and direction of crack propagation are significantly affected can be simply defined near a particle as a function of the crack-particle geometry and elastic mismatch. A wide range of elastic combinations was examined with the result that for any significant crack deflection to occur away from the particle the magnitude of the first Dundurs parameter, $|\alpha|$, must be greater than ~ 0.2. Numerical results show good agreement with experimental fatigue crack path data.

1. Introduction

Potential structural and high performance materials are often toughened by mechanisms involving increased energy dissipation based on crack-particle interaction, therefore cracks must intersect or pass very near the particles in order to realize an improvement in mechanical properties. For example, in zirconia-stabilized ceramic systems, residual stresses around the zirconia particles combine with stress-induced, martensitic zirconia phase transformations to increase fracture resistance [1–4]. Other examples involve the residual thermal stresses near particles which retard crack propagation and fracture [5–10]. For fiber- or whisker-reinforced ceramic composites such as SiC-reinforced alumina the main toughening mechanisms are proposed to be crack bridging, fiber pull-out and crack deflection [11–13]. Some composites combine ductile, softer second-phase particle inclusions in a brittle matrix to attract cracks and increase toughness through localized plastic energy dissipation combined with subsequent crack-bridging mechanisms [14–17]. In a random microstructure, the number of crack-particle intersections is statistically proportional to the inclusion volume fraction. Increasing the number of intersections through crack deflection must therefore increase the toughening effects. It is thus advantageous to generalize the range of crack-particle interaction so that when designing a material microstructure or analyzing fracture properties, consideration can be given to the interaction effects which extend past the particle boundaries.

The interaction between a crack and a material inhomogeneity such as a hole or a particle has previously received a great deal of analysis [18–29]. These and many other works have analyzed quasi-static crack trajectories and driving forces analytically, numerically and experimentally. In every case, a deterministic geometry and material combination was used in which the crack-particle interaction was strong. However, no extension has been made to simply define the zone in which interaction occurs for an unspecified crack-particle geometry

or general material combination. One statement is that for a cracked plate which contains a hole, the interaction zone extends beyond the hole a distance roughly equal to the diameter [19]. Only an empirical basis was given for this statement and no mention was made of other geometrical factors such as crack length or crack-particle orientation. For models containing cracks near particles, no similar, simply applicable generalization has been given.

The objective of the current work is therefore to define a crack-particle interaction zone for non-homogeneous bodies as a function of geometry and elastic mismatch in which quasi-static crack deflection will occur or crack driving force will be significantly changed. Crack trajectories will not be strictly analyzed, rather a region in which crack deflection occurs will be defined based on the geometric and elastic parameters of the system. Finally, in order to verify the accuracy of the general zone prediction, calculated and experimentally observed points of crack deflection will be compared.

2. Model

The crack-particle interaction in a composite material will be quantified using a simplified plane strain model of a single crack and particle as shown in Fig. 1. The presence of additional particles will be neglected because it is believed that only the particle in the immediate neighborhood of the crack tip will strongly influence propagation. For maximum generality, internal and edge cracks with traction free crack surfaces are examined using both the Boundary Element Method and the Finite Element Method, respectively. The wide range of crack and particle geometries investigated are intended to reveal the effects of crack length a, particle size R, crack-particle separation distance d, and particle orientation angle ϕ during the initial stages of fracture in an actual composite. The modelled area is $W_e \sim 25\,\text{mm}$ by $H_e \sim 50\,\text{mm}$ for the width and height of the edge cracked specimen, and $W_i \sim 200\,\text{mm}$ by $H_i \sim 200\,\text{mm}$ for the width and height of the internal crack specimen. Quantities a, d and R are in the range between 0.1 and 4 mm. Because the most critical loading for crack propagation is typically the opening mode, only this far field loading configuration will be considered. Displacement boundary conditions for the edge-cracked specimen are therefore: $u_x(x = 0, y = 0) = u_y(x = 0, y = 0) = 0, u_x(x > 0, y = 0) \neq 0, u_y(x > 0, y = 0) = 0, u_x(x = 0, y = H_e) = 0, u_x(x > 0, y = H_e) \neq 0$ and $u_y(x \geqslant 0, y = H_e) = U_{\text{ext}}$ where U_{ext} is an input constant.The vertical edges of the model $(x = 0, y \geqslant 0)$ and $(x = W_e, y \geqslant 0)$ are not restricted in their motion. These conditions correspond to a pure mode I loading. The internal crack model is loaded by a far-field, uniaxial stress boundary condition $\sigma_{yy}(x \geqslant 0, y = 0) = \sigma_{\text{ext}} = \sigma_{yy}(x \geqslant 0, y = H_i)$ while the other surfaces are traction free. In both geometries the particle and matrix are perfectly bonded so that at the interface $u_x(m) \equiv u_x(p)$ and $u_y(m) \equiv u_y(p)$. Under this interfacial bonding condition, stress components normal to the interface must be continuous while those tangent to the interface can be discontinuous. The two geometries will also show the importance of the interaction effects between the specimen edge and the particle. No stress field disturbances due to thermal or residual stresses will be considered. All stresses are assumed to remain in the elastic range of both the matrix and the inclusion. Finally, because mesh resolution between the crack tip and inclusion is critical, the mesh is refined until the results converge to a constant value.

Consideration must also be given to the possible elastic constants of the particle and matrix because modern engineering materials are often nonhomogeneous mixtures of phases. To

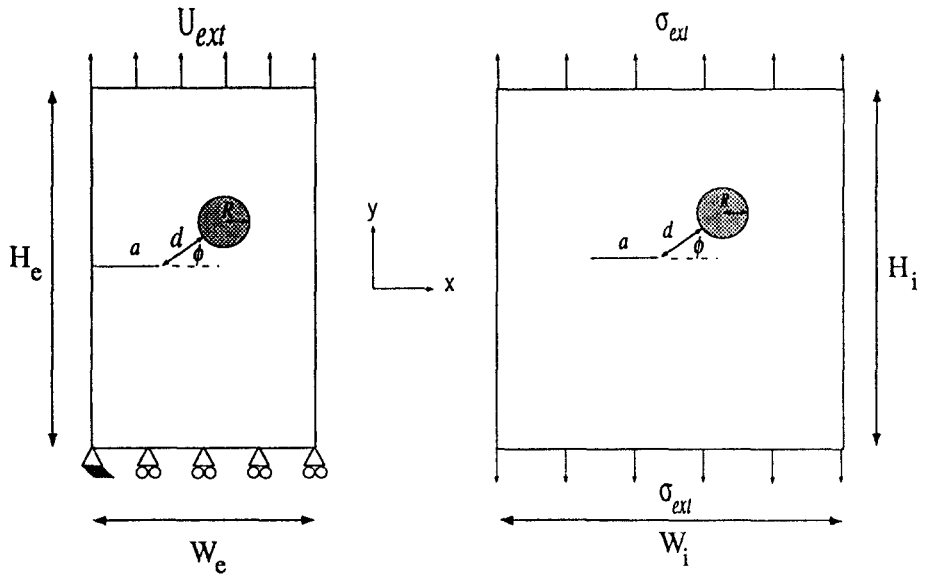

Fig. 1. Schematics of Finite Element (edge crack) and Boundary Element (internal crack) model showing the geometry of the problem and boundary conditions.

characterize the elastic mismatch between the particle and the matrix, the Dundurs parameters α and β are conveniently defined in plane strain as

$$\alpha = \frac{E_i - E_m}{E_i + E_m} \tag{1}$$

and

$$\beta = \tfrac{1}{2}\alpha\frac{(1-2\nu)}{(1-\nu)}, \tag{2}$$

where E_m and E_i are the Young's moduli of the matrix and the inclusion, and ν is the Poisson's ratio of both materials if $\nu_i \sim \nu_m \sim \nu$ [30]. If the Poisson's ratios of the matrix and inclusion are sufficiently different that these simplified expressions cannot be used, the more complicated expressions must be used [31]. The limiting values of α and β have been previously shown to be $-1 \leqslant \alpha \leqslant 1$ and $(\alpha - 1)/4 \leqslant \beta \leqslant (\alpha + 1)/4$ due to the limited values of $0 < \nu < 0.5, \mu_i/\mu_m > 0$ and $k = 3 - 4\nu < 3$ for plane strain conditions [31, 32]. Typical engineering composites have α and β values that range from $-0.6 < \alpha < +0.6$ and $\beta = \frac{1}{4}\alpha \pm 0.1$ [33]. A hole in any material is specified by $\alpha = -1$ because void space cannot support load. The α values examined here will be in the range $-1 < \alpha < -0.15$ which corresponds to particles which are softer than the matrix and thus attract cracks. Positive values of α will not be considered because previous investigations on similar geometries have shown that changing only the sign of α results in essentially the same level of interaction between a crack and a particle with a reversed sense [34]. Specifically, for the geometry of $d = 0.8$ mm, $R = 1.6$ mm, $a = 0.8$ mm and $\phi = 22.5°$, if $\alpha = +0.6$, then for a given external load, K_{I} and K_{II} are 95.8 and -2.6 MPa $\sqrt{\mathrm{mm}}$, respectively, but if $\alpha = -0.6$, K_{I} and K_{II} are 136.3 and 2.8 MPa $\sqrt{\mathrm{mm}}$, respectively [35].

3. Method

In order to define a zone of interaction and deflection near a particle, the geometry and elastic parameters must be analyzed in terms of their effects on crack driving force and crack propagation angle. The extent of interaction will be gauged by normalizing the maximum energy release rates for the composite by the maximum energy release rate for the homogeneous case $G_{\max}^{\text{comp}}/G_{\max}^{\text{homo}}$. The proper determination of the total energy release rates and stress intensity factors is thus critical. The modified virtual crack closure method is used to determine the relative mode I and mode II energy release rates G_{I} and G_{II} at the crack tip as a function of possible crack propagation angles in the edge-cracked geometry [36, 37]. The criterion of maximum total energy release rate is applied to determine the direction of crack propagation. This method is equivalent to the criterion of maximum circumferential stress, $\sigma_{\theta\theta}$, or minimum K_{II}. Friction on the crack faces is neglected therefore the mode II energy release rate as calculated will likely be an overestimation of actual values. The BE method is used to directly calculate both K_{I} and K_{II} values for the internal crack geometry [38, 39]. The quasi-static crack propagation angle θ^{cr} will subsequently be determined by the K_{I} and K_{II} values according to the equation [40]

$$\theta^{\text{cr}} = \arccos\left[\frac{3K_{\text{II}}^2 + K_{\text{I}}\sqrt{K_{\text{I}}^2 + 8K_{\text{II}}^2}}{K_{\text{I}}^2 + 9K_{\text{II}}^2}\right]. \tag{3}$$

Direct comparison of internal and edge cracked data is possible following the calculation of normalized energy release rate from the stress intensity factors as

$$\frac{K_{\text{I}}^2 + K_{\text{II}}^2}{K_{\text{I,app}}^2} = \frac{G_{\max}^{\text{comp}}}{G_{\max}^{\text{homo}}}, \tag{4}$$

where $K_{\text{I, app}}$ is the externally applied mode I stress intensity factor in the homogeneous case.

As an example of this series of calculations consider crack propagation in a body such as is shown in Fig. 1 without an inclusion. Following the application of a uniaxial boundary displacement U_{ext} normalized components of mode I and II energy release rate are shown as a function of angle as calculated by FEM in Fig. 2. As expected from symmetry considerations, the orientation of the maximum energy release rate $\theta^{\max}$ is at 0° and the crack propagates perpendicular to the loading axis. Notice the total energy release rate curve is very flat around the maximum and a value greater than or equal to 98 percent of $G_{\text{tot}}^{\max}$ is observed over a range of roughly 20 degrees. This shows that slight variations in fracture resistance may greatly affect the actual cracking angle. Such deviations may physically arise from features such as component interfaces, grain boundaries or specific crystallographic planes. However, a simple continuum model which ignores these effects will be considered in all calculations here.

4. Results

The effects of crack-particle separation on the crack driving force are the most significant and will thus be examined first by varying d while the other geometrical parameters are held constant. Figures 3a and 3b show that the particle ($R = 1.6\,\text{mm}, \alpha = -0.35$) must be brought to within $\sim 2\,\text{mm}$ ($\phi = 22.5°$) of the crack tip ($a = 0.8\,\text{mm}$) in order to

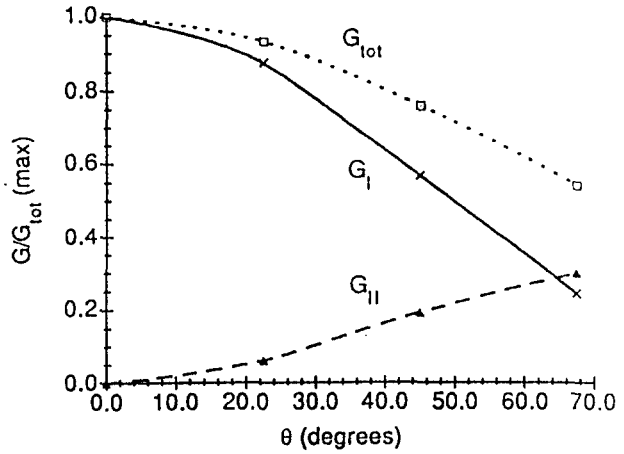

Fig. 2. Mode I, II and total energy release rates, B, for a cracked body loaded in uniaxial tension. The values are normalized to the maximum, total energy release rate for relative comparison.

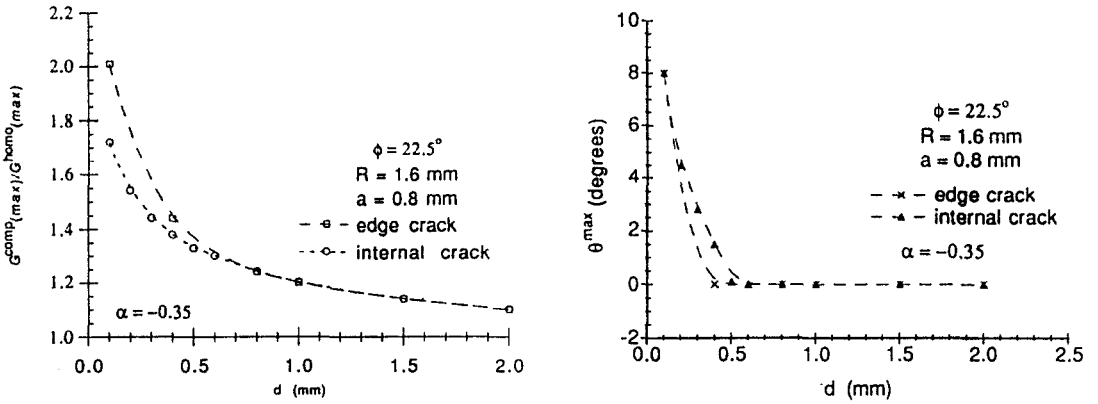

Fig. 3. Crack driving force results for constant crack length and particle size for a particle which is a variable distance from the crack tip. (a) Maximum energy release rate values. (b) Orientation of maximum energy release rate.

affect a significant change in the maximum total energy release rate and less than ~ 0.4 mm to cause a shift in $\theta^{\max}$, or θ^{cr}. A slight difference exists between the internal and edge cracked geometries because of the edge-particle interaction. However, for either case, these plots indicate that 2 critical distances, $d_{\text{crit}} \sim 2$ mm and ~ 0.4 mm, can be defined for calculating crack-particle interaction. Only the smaller will be considered further because crack deflection is of current interest. The effects of ϕ, R, a and α on d_{crit} will be shown below.

The influence of particle orientation is revealed through a series of similar energy release rate calculations for geometries in which ϕ is variable and a, d, R and α are held constant. The small crack-particle separation, $d = 0.1$ mm, is used in order to observe effects which might not occur for larger separations. Results plotted on Fig. 4 for $\alpha = -0.35$ show the expected result that a particle has the strongest influence on the crack driving force when situated symmetrically ahead of the crack. Again, there is a difference between the edge cracked and internal cracked data due to edge-particle interaction. The crack exhibits a tendency to deflect toward the particle as ϕ increases but crack deflection in this case ($\phi < 70°$) is never greater

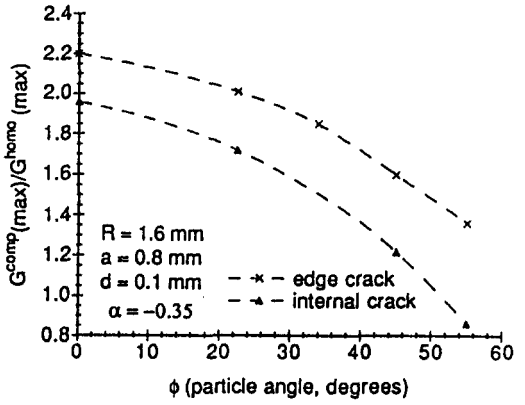

Fig. 4. Normalized maximum energy release rate results for various particle orientation angles shown for both internal- and edge-cracked geometries. The particle has the largest effect when placed directly in the crack path.

than 15°. The remaining factors of crack length and particle size as related to crack driving force and deflection angle were subsequently examined and will be plotted below.

Summarizing the calculations for the various geometries in a consistent manner requires not only an indicator for crack driving force, but also a single dimensionless function of the geometric variables to measure the relative scale of the crack, particle and separation distance. For example, efforts to define the geometry of similar problems as a function of two variables, such as normalized crack length and crack-particle separation, a/R and d/R, have been successful, although one of the two ratios must be constant for unambiguous comparisons of results [21, 34]. Here and in Part I of this investigation it has been shown that data fitted to a single parameter of the form $(d(d+a)/aR)f(\phi)$ are readily compared in various geometries [41]. The ratio $d(d+a)/aR$ effectively groups the geometric factors, and the function $f(\phi)$ is introduced here to include the influence of particle orientation. Of the many functions that could be used for the angular dependence, $f(\phi) = 1/\cos\phi$ is chosen for its simplicity and consistency with results in the range of $0 < \phi < 70°$. Figure 5 shows the results for both internal and edge cracked configurations over a wide range of all geometric variables under this format for $\alpha = -0.35$. Abscissa values are in the range of $0.1 < x < 4.5$ where

$$x = \frac{d(d+a)}{aR\cos\phi}$$

and a, d, R and ϕ are defined above. The data now show the single trend that increasing abscissa values correspond to decreasing ordinate values. Although the data now fall into a consistent band, the parameter is not able to completely focus the wide range of investigated geometries into a single, well-defined curve.

In order to make this analysis applicable to many different material combinations, all calculations above were repeated for various elastic combinations as plotted on Fig. 6. The magnitudes of the slopes and y-intercepts of lines fitted to the data increase with the magnitude of α, as expected from the fact that crack-particle interaction must increase with elastic mismatch. However, for $|\alpha| \geqslant 0.35$ two distinct regimes emerge with the transition at $x \sim 1.0$. In the $x > 1$ regime, the driving force shows a weak dependence on x while the opposite is seen for $0.1 < x < 1.0$. The case of $\alpha = -1$ applies to the maximum elastic mismatch and calculations reflect this extreme in crack driving force.

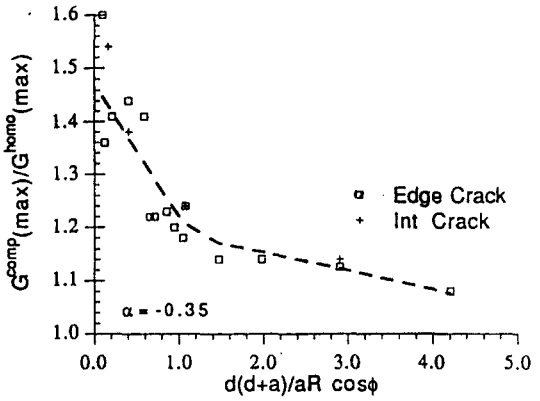

Fig. 5. Summary of normalized maximum energy release rata data plotted as a function of a new geometrical parameter including crack length, particle orientation. A single trend is seen for a wide variety of modelled geometries.

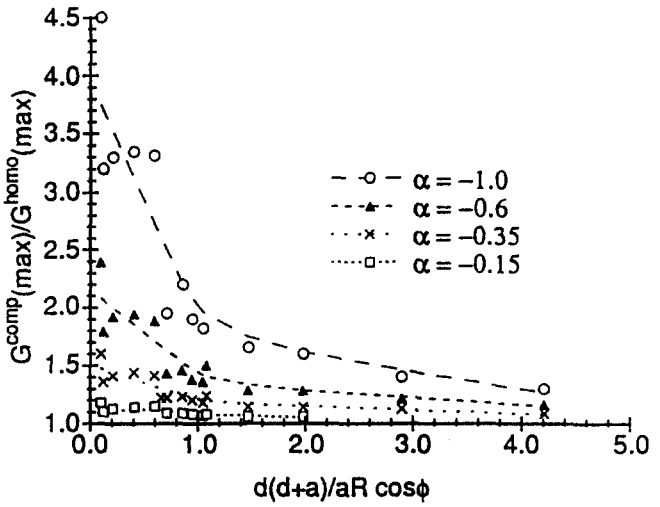

Fig. 6. Normalized crack driving force data plotted for various values of α as a function of the dimensionless geometric parameter. The data for $\alpha = -1$ correspond to the extreme case of a crack approaching a hole.

5. Discussion

In order to analyze crack deflection and its effect on composite toughness, the underlying forces which drive a crack out of its plane must be first examined. If the crack tip is in a homogeneous medium, the crack will follow the direction of maximum energy release rate as described by (3) provided that the driving force is greater than the material fracture resistance. It is seen in Fig. 3 that this condition is satisfied in the current model if the maximum energy release rate is greater than the homogeneous driving force by roughly 35 percent. However, driving force increase alone is no valid crack deflection criterion. In the case of a crack symmetrically approaching a hole, the maximum energy release rate may be higher than the homogeneous case by a factor of 2, as shown in Fig. 4, with no crack deflection. It must be clarified that the current analysis is primarily concerned with cracks that do not symmetrically approach particles, $20° < \phi < 70°$. For these nonsymmetric cases it is apparent that a given change in driving force coupled with a large asymmetry is a reasonable crack deflection criterion. This

will be shown to be true by means of a comparison to experimental results below. Figures 3 and 4 also show that the driving forces for internal and edge cracked geometries can be significantly different if the particle is less than $\sim \frac{1}{2}R$ from the specimen edge. This difference is eliminated by the normalizing geometrical parameter as in Fig. 5.

Given the empirical criterion for crack deflection as above, it now remains to define a crack-particle geometry which satisfies this criterion, thereby defining a zone in which crack deflection will occur near a particle. It can be seen by the smooth monotonic trends in Figs. 5 and 6 that an increasing x-value corresponds to a decreasing particle effect. Therefore geometries with correspondingly low x-values will exhibit crack deflection while those with high x-values will not. The question now arises as to the threshold x-value at which crack deflection begins. Recall that the driving force must be increased by $\sim$ 35 percent over the homogeneous case and the particle-crack orientation angle must be sufficiently high for a crack to be deflected. An ordinate value of $\sim$ 1.35 can thus be used to define a threshold configuration for crack deflection as determined from the data. Figures 5 and 6 show the threshold values of $x \sim 0.6$ for $\alpha = -0.35, x \sim 2$ for $\alpha = -0.6$ and $x \sim 4$ for $\alpha = -1$. It is also reasonable to conclude that for $|\alpha| \leqslant 0.2$, the limited difference in the driving force implies that little or no crack deflection is possible in the $0.1 < x < 4.5$-range. The size of the deflection zone, d, is therefore determined as a function of angle, $20° < \phi < 70°$, by the magnitude of the threshold, or critical x-value and the particle radius according to the relation

$$\left[x = \frac{d(d+a)}{aR\cos\phi}\right]_{\frac{G^{\text{comp}}}{G^{\text{homo}}}\sim 1.35} = x_{\text{crit}} \tag{5}$$

and thus

$$d = \tfrac{1}{2}a\left(-1 + \sqrt{1 + \frac{4x_{\text{crit}}}{a} \cdot R\cos\phi}\right). \tag{6}$$

The quantity that remains unknown is the crack length. Because the initial stages of fracture are of primary interest, a crack length on the order of the particle size will be taken, as indicated schematically in Fig. 1.

The accuracy of the deflection zone calculated in this analysis can now be demonstrated by comparing experimental and numerical results. Previously published experimental results are reproduced in Fig. 7, showing an enlarged section near the hole in a side-cracked specimen from 3 different experimental fatigue crack trajectories [18, 19]. This literature is chosen because the modelled geometry and loading conditions as well as the quasi-static crack advance, Fig. 1, and the experimental conditions are the same. Furthermore, the material used experimentally, PMMA, was observed to have only a small crack-tip plastic zone. The 3 cases refer to cracks which approach the hole 2.5 mm (I), 3.5 mm (II), and 4.5 mm (III) above the center of the hole with $R = 1.5$ mm. The boundary of the zone is shown by the cross-hatched band as calculated using (5) and (6), given the hole size and crack lengths which correspond to the actual edge-cracked configuration. Case I shows that the zone boundary is crossed by the crack but only slight crack deflection occurs until $\phi \sim 60°$. For Case II, crack deflection begins when the boundary is reached because crack driving force and ϕ are both sufficiently high. The crack in Case III never crosses the zone boundary and no significant crack deflection is expected or seen. It is therefore reasonable to conclude that if a crack crosses into the

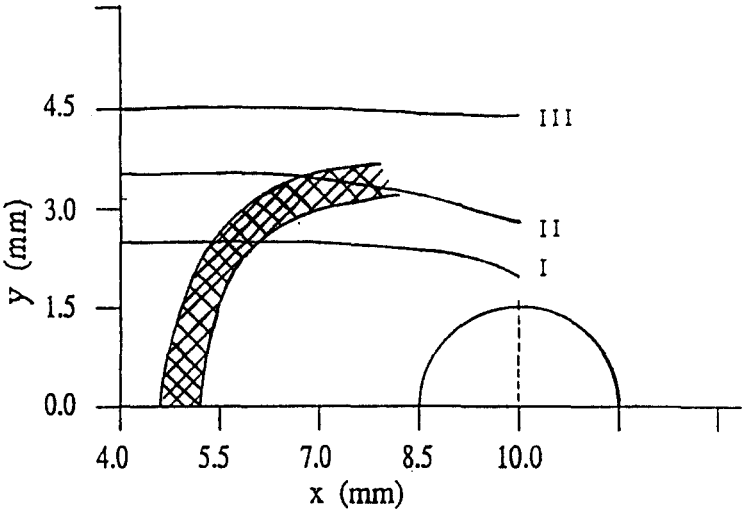

Fig. 7. Good agreement is seen between experimental data for three cracks approaching a hole and the deflection zone defined here. If a crack passes into the deflection zone it will experience significant crack deflection near the hole when the orientation angle, ϕ, is sufficiently high.

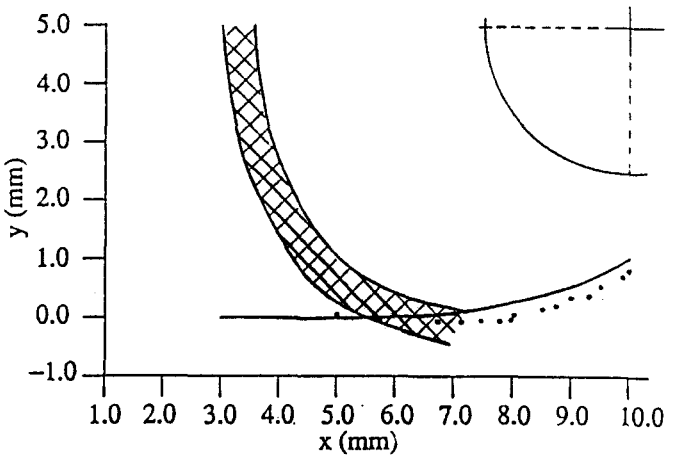

Fig. 8. Experimental and calculated crack trajectory data show good agreement with the generalized zone boundary near a hole in a CCT specimen.

deflection zone, significant crack deflection will occur either directly upon crossing or when ϕ is roughly greater than 40°. The correlation here is considered very good considering the analysis of Rubinstein who showed that the actual crack deflection observed experimentally can be as much as 15 degrees away from the calculated maximum energy release rate angle [18]. Another comparison is given in Fig. 8 for a Center Cracked Tension (CCT) specimen as calculated for $\alpha = -1$ [20]. This case is given as an example because experimentally the material and geometry are similar to the model. Good agreement is again seen between the zone boundary and the onset of calculated crack deflection, while the observed crack deflection lags slightly behind. The discrepancy is due to a reduced K_{II} at the crack tip which results from crack surface friction. The salient feature in these comparisons is that if the crack crosses the zone boundary significant deflection is expected and observed.

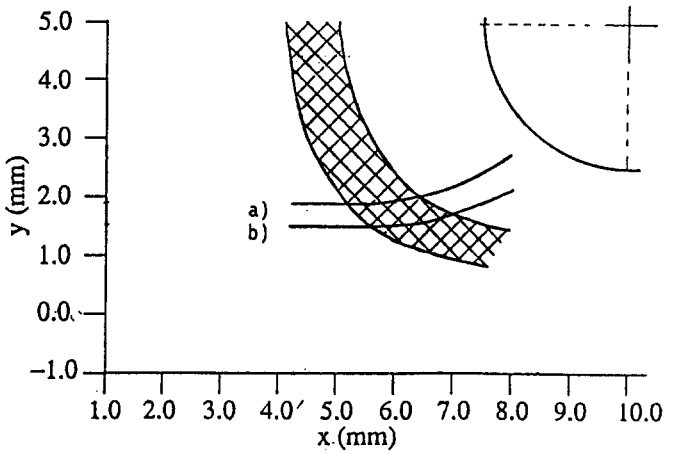

Fig. 9. Two crack trajectories, (a) and (b), near particles in a CCT specimen ($\alpha = -0.6$). Neither crack begins in a plane which intersects the particle. However, because both cracks cross the zone boundary, deflection is expected and calculated.

The validity of the zone predictions can also be verified for the case of a crack approaching a particle rather than a hole. Figure 9 shows the geometry as in Fig. 8 with two calculated crack paths for cracks which approach a particle ($\alpha = -0.6$) from different starting planes marked as (a) and (b). Notice that the crack deflection zone as calculated using an x_{crit}-value of ~ 2 does not extend as far into the matrix as for the case of a hole. The BEM-calculated crack paths verify that the general zone approximation is again accurate for this combination of materials, although experimental data is not available. This is a very powerful result because now the zone of crack deflection can easily and accurately be determined for a general crack-particle geometry for many material combinations without the use of more difficult and time-consuming, conventional FE or BE method calculations.

The deflection zone calculated here will apply most accurately to the initial stages of fracture where the crack length is roughly on the order of the particle size as shown in the examples above. This is perhaps the most critical phase of failure. Stable subcritical microcrack growth has been shown to contribute significantly to the strength of polycrystalline alumina while increasing the macroscopic steady state K_{Ic} has a smaller effect on strength [42]. If other brittle matrix composites behave similarly, then strength, toughness and ductility models would necessarily require consideration of increased microcrack stability through crack deflection.

Based on the fact that a crack is able to deflect toward and intersect particles which are well out of its original plane, overall composite toughening models must be carefully reconsidered. For example, a single particle ($\alpha = -0.6$, Fig. 9) with radius R has a deflection zone profile which is ~ 60 percent larger than the diameter. Therefore composite toughening models which assume a planar crack front and a number of crack-particle intersections proportional to the volume fraction will be neglecting this very significant increase in effective particle size. Specifically, the deflection effects will be responsible for a warped or twisted crack front as well as a significant increase in the number of crack-particle intersections. Note that on Fig. 9, both cracks (a) and (b) are calculated to strike the particle although they begin on planes which do not intersect the inclusion. The most significant influence on crack stabilization will likely be the increased amount of energy dissipation (plastic deformation or phase transformation)

which accompanies the increased number of particle-crack intersections. Additionally, when a crack front is twisted out of the plane normal to the applied stress or pinned between particles a locally decreased mode I stress intensity factor is seen [23, 24, 43, 44]. The decreased K_I at the crack tip will be reflected as an overall increase in K_{Ic} and failure strength. Finally, the greater number of particles which are intersected for a deflected crack front than for a planar crack indicates that more load will be carried behind the crack tip and that the wake zone will play a larger role.

6. Summary and conclusions

A general basis has been given to determine the zone boundaries near particles within which quasi-static cracks are deflected due to the local stress field disturbances. Global material toughness and strength will be strongly influenced by these deflection effects. In the initial stages of failure microcracks can be stabilized by the particles to an extent greater than the volune percent alone indicates because particles are effectively 'larger' due to their ability to attract cracks which would otherwise not intersect them. Results show good agreement with experiments and specific numerical examples. The method accounts for variable crack length, particle diameter, elastic mismatch and crack-particle separation and orientation. The distance which the zone extends into the matrix is calculated using a critical value of a dimensionless geometric parameter, $x_{crit} \sim 0.7$, 2.0 and 4.0 for $\alpha = -0.35, -0.6$ and -1.0, respectively. Below $|\alpha| < 0.2$, no significant crack deflection is expected. The empirically-based criterion which determines the zone boundary is defined as the point where the crack driving force increases roughly 35 percent over the homogeneous case and the particle orientation angle, ϕ, is simultaneously greater than approximately 20°.

The limitations of this work are that a continuum model and macroscopic examples are used to study the interaction between a crack and a particle in which no grain-based or atomistic effects are considered, while for a very small particle these effects may be large. Also, because only a single, circular particle was modelled, these zones are not expected to be accurate for particles that are highly elongated or have sharp corners, or have other particles in close proximity. Differences may also arise between observations and predictions due to the simplification of plane strain compared to an actual 3-D particle. Finally no consideration has been given to the effects of plasticity. Particle plasticity will increase the size of the deflection zone as calculated here due to the fact that the stress in the plastically deformed particle will be much lower than stress calculated using a purely elastic relationship. Matrix plasticity will most likely modify the results given here.

Acknowledgments

Financial support for PL as a visiting scientist from Professors H . Fischmeister and E .Arzt as well as the Max-Planck-Gesellschaft is gratefully acknowledged.

References

1. D.L. Porter and A.H. Heuer, *Journal of the American Ceramic Society* 60 (1977) 183.
2. T.K. Gupta, F.F. Lange and J.H. Bechtold, *Journal of Material Science* 13 (1978) 1464.
3. F.F. Lange, in *Proceedings of 3rd International Conference on Mechanical Behavior of Materials*, Vol 3, K.J. Miller and R.F. Smith (eds), Pergamon Press (1980) 45.
4. *Science and Technology of Zirconia*, II, M. Ruhle, N. Claussen and A. Heuer (eds) (1982).
5. A.G. Evans, *Journal of Material Science* 9 (1974) 1145–52.

6. W. Kreher and R. Janssen, *Journal of European Ceramic Society* 10 (1992) 167–73.
7. P. Lipetzky and W. Kreher, *Mechanics of Materials* 20 (1995) 225–240.
8. M. Taya, S. Hayashi, A. Kobayashi and H. Yoon, *Journal of the American Ceramic Society* 73 (1990) 1382–91.
9. D. Baril, S. Tremblay and M. Fiset, *Journal of Material Science* 28 (1993) 5486–94.
10. R. Brett and P. Bowen, *Composites* 24 (1993) 177–83.
11. P.F Becher and G.C. Wei, *Journal of American Ceramic Society* 67 (1984) C267–C271.
12. F.F. Lange, *Fracture Mechanics of Ceramics*, Vol 4, R.C. Brandt, D.P. Hasselman, and F.F. Lange (eds), Plenum Press (1978).
13. B. Budiansky, J.W. Hutchinson and A.G. Evans, *Journal of the Mechanics and Physics of Solids* 34 (1986) 167–189.
14. V.D. Krstic, P.S. Nicholson and R.G. Hoagland, *Journal of the American Ceramic Society* 64 (1981) 499–504.
15. V.D. Krstic, *Philosophical Magazine* A, 48 (1983) 695–708.
16. L.S. Sigl, P.A. Mataga, B.J. Dalgleish, R.M. McMeeking and A.G. Evans, *Acta Metallurgica* 36 (1988) 945–953.
17. M. Bannister, H. Shercliff, G. Bao, F. Zok and M. Ashby, *Acta Metallurgica* 7 (1992) 1531–37.
18. A. Rubinstein, *International Journal of Fracture* 47 (1991) 291–305.
19. A. Chudnovsky, K. Chaoui and A. Moet, *Journal of Materials Science Letters* 6 (1987) 1033–38.
20. Z. Knesl, *Acta Technica CSAV* 5 (1987) 603–20.
21. F. Erdogan, G.D. Gupta and M. Ratwani, *Journal of Applied Mechanics* 41 (1974) 1007–1013.
22. S.A. Meguid, *Engineering Fracture Mechanics*, Elsevier, NY (1989) 158.
23. D.J. Green, P. Nicholson and J. Embury, *Journal of Material Science* 14 (1979) 1413–20.
24. Ibid., 1657–61.
25. W. Muller and S. Schmauder, *International Journal of Fracture* 59 (1993) 307–43.
26. W. Muller and S. Schmauder, *International Journal of Solids and Structures* 29 (1992) 1907–18.
27. F. Erdogan and G. Gupta, *International Journal of Fracture* 11 (1975) 13–27.
28. F. Lange, *Philosophical Magazine* 22 (1970) 983–92.
29. P. Trusty and J. Yeomans, *Ceramic Engineering Science Proceedings* 14 (1992) 908–13.
30. M. Meyer and S. Schmauder, *Zeitschrift Metallkunde* 83 (1992) 524–27.
31. J. Dundurs, *Journal of Applied Mechanics* 36 (1969) 650–52.
32. D. Bogy, *Journal of Applied Mechanics* 38 (1971) 377–86.
33. T. Suga, G. Elssner and S. Schmauder, *Journal of Composite Materials* 22 (1988) 917–21.
34. W. Muller, S. Schmauder, A.G. Evans and R.M. McMeeking, *International Journal of Fracture*, in press.
35. Z. Knesl and H. Maschke, *Kovove Materialy* 27 (1989) 175.
36. F.G. Buchholz and H. Richard, *Advances in Fracture Research*, Vol 3, K. Salama (ed.), Pergamon Press (1989) 2301–2308.
37. E.F. Rybicki and M.F. Kanninen, *Engineering Fracture Mechanics* 9 (1977) 931–938.
38. J.C. Brebbia, J.C.F. Telles and L. Wrobel, in *Boundary Element Technique-Theory and Applications*, NY (1984).
39. H. Maschke, *Technische Mechanik* 6 (1985) 17.
40. F. Erdogan and G.C. Sih, *ASME, Journal of Basic Engineering* 85 (1963) 519–527.
41. P. Lipetzky and S. Schmauder, *International Journal of Fracture* 65 (1994) 345–58.
42. A. Krell and W. Pompe, *Materials Science and Engineering* 89 (1987) 161–68.
43. K.T. Faber and A.G. Evans, *Acta Metallurgica* 31 (1983) 565–76.
44. Ibid., 577–84.